Research Article | Vol. 33, No. 6 / 24 Mar 2025 / Optics Express 13376
Optics EXPRESS

Enhancing the Swanepoel method: precise envelope detection of thin-film transmission spectra

MANUEL BALLESTER,[1,*] ALMUDENA P. MARQUEZ,[2] SANTIAGO LOPEZ-TAPIA,[3] SUSANA FERNANDEZ,[4] JOHN BASS,[5] DORIAN MINKOV,[6] CHRISTOPH WUERSCH,[7] FLORIAN WILLOMITZER,[5] EMILIO MARQUEZ,[8] AND AGGELOS K. KATSAGGELOS[1,2]

[1]*Computer Science Department, Northwestern University, Evanston, IL 60208, USA*
[2]*Department of Mathematics, Faculty of Science, University of Cadiz, 11510 Puerto Real, Spain*
[3]*Department of Electrical and Computer Engineering, Northwestern University, Evanston, IL 60208, USA*
[4]*CIEMAT, Avenida Complutense 40, 28040 Madrid, Spain*
[5]*Wyant College of Optical Sciences, University of Arizona, Tucson, AZ 85721, USA*
[6]*Research Section (NIS), Technical University, Sofia 1000, Bulgaria*
[7]*Institute for Computational Engineering ICE, OST, Eastern Switzerland University of Applied Sciences, Switzerland*
[8]*Department of Condensed-Matter Physics, Faculty of Science, University of Cadiz, 11510 Puerto Real, Spain*
[*]*manuelballestermatito2021@u.northwestern.edu*

Abstract: The Swanepoel method is a widely used optical technique for characterizing thin films through normal-incidence transmission measurements. A critical step in this approach involves extracting the upper and lower envelopes of the measured oscillatory spectrum. By analyzing the transmission spectrum and its corresponding envelopes, the Swanepoel procedure enables precise determination of the film refractive index and extinction coefficient. However, even minor inaccuracies in envelope construction can propagate significant errors into the final characterization results. To address this challenge, we present what we believe to be a novel physics-informed optimization algorithm for envelope detection. Our mathematical model reformulates the envelope detection problem as a global optimization task that enforces the physical properties of the Swanepoel envelopes. Extensive validation on fifty randomly generated transmission spectra demonstrates unprecedented accuracy: the method achieves root-mean-square errors (RMSE) below 0.10% for the upper envelope and 0.06% for the lower envelope (more than doubling the accuracy of current state-of-the-art approaches). Furthermore, the proposed model has been assessed with two experimental transmission spectra, demonstrating its robustness and accuracy with real noisy data. We have developed an open-source Python software package (see text below). This software includes not only our innovative envelope construction algorithm but also additional envelope drawing algorithms for comparison and an efficient implementation of the Swanepoel method, enabling complete optical characterization of thin films.

© 2025 Optica Publishing Group under the terms of the Optica Open Access Publishing Agreement

1. Introduction

Thin solid films are indispensable components in a vast array of optical systems and optoelectronic devices. *Semiconductor* thin films are foundational in the fabrication of transistors, diodes, and photodiodes [1–4]. For instance, silicon thin films are extensively employed for cost-effective optical sensors [5–7] and solar cells [8–10] due to their efficient light-absorbing capabilities and

#553824 https://doi.org/10.1364/OE.553824
Journal © 2025 Received 23 Dec 2024; revised 14 Feb 2025; accepted 17 Feb 2025; published 14 Mar 2025

Optics EXPRESS

scalable manufacturing processes. *Conductive* thin films are highly valued for their exceptional electrical conductivity and reflectivity, enabling their use in electrode fabrication, optical mirrors, protective coatings, and forming electrical connections within integrated circuits [11–14]. In particular, transparent conductive films play a crucial role in the development of touch panels and liquid crystal displays. *Dielectric* thin films, engineered with specific refractive indices and thicknesses, create thin-film capacitors, act as insulating layers, and form anti-reflection coatings that enhance light transmission [15,16]. Dielectric coatings are integral to optical instruments such as lenses, bandpass filters, dichroic mirrors, and beamsplitters, providing precise control over light propagation and wavelength selection [17].

The manufacturing processes of the thin film material critically influence their optical properties [18,19], which in turn affect the performance of the target devices. Therefore, precise determination and control of these properties are essential for optimizing the mentioned optoelectronic devices and optical systems. By performing optical characterization of thin films, we can obtain their refractive index and extinction coefficient, denoted as $n(\lambda)$ and $k(\lambda)$, respectively. These wavelength-dependent optical properties combine to form the complex refractive index ($\mathbf{n} = n + ik$) or the complex dielectric function ($\boldsymbol{\epsilon} = \mathbf{n}^2$). The dielectric function offers insights into the optoelectronic properties of the film material and allows for precise quantification of the electronic transitions. Therefore, one can extract information about critical parameters such as bandgap energy [20–22], molecular disorder [23], and charge mobilities [24].

A myriad of techniques exist to determine the optical properties of thin solid films. Spectroscopic analyses are common [25–27] for characterizing materials across a broad spectral range (UV-VIS-NIR), employing transmittance, reflectance, or ellipsometric measurements. Spectroscopic ellipsometry, in particular, is a commonly employed technique that measures the changes in the polarization state of light upon reflection, at varying angles of incidence. This technique can produce a comprehensive phase-sensitive dataset, allowing for the precise characterization of complex film structures, including surface roughness, thickness variations, multilayer systems, and anisotropic materials. In contrast, conventional spectrophotometric techniques, which rely on direct measurements of the transmitted or reflected light intensity, offer a simpler approach for obtaining an overall average estimation of a material's optical properties. While spectrophotometry is less sensitive to fine structural variations, it remains a widely used method due to its straightforward implementation and broad applicability. The present study focuses on characterizations derived solely from normal-incidence transmission spectra, which are optimal for assessing material properties at photon energies below the optical bandgap, where moderate to low absorption enables highly sensitive transmission data. Typically, the thin-film material is deposited on a thick glass substrate with negligible absorption ($k_s \approx 0$) and a near-constant refractive index (n_s) in the spectral region of interest (ROI). Before the thin-film preparation, the transmittance of the substrate alone, denoted $T_s(\lambda)$, is sequentially collected over different wavelengths using a spectrophotometer, allowing us to easily account for the effect of the substrate when analyzing the whole sample. As illustrated in Fig. 1(a), the transmittance of the complete sample (thin film over the substrate), $T(\lambda)$, is subsequently measured.

The Swanepoel method and other characterization approaches: In 1983, Ryno Swanepoel [28] introduced an numerical procedure, widely known nowadays as the *Swanepoel method* or the *Envelope method*, to determine the thin-film thickness d and its optical functions (n and k) at specific wavelengths. These particular wavelength of interest are called *tangent points* (see Fig. 1(c)), as they appear where the transmission spectrum intersects (touch but not cross) its upper or lower envelopes. Although earlier envelope-based approaches had been developed before Swanepoel [29–31], his contribution significantly enhanced the precision and applicability of the technique, leading to a widespread algorithm extensively used today. Renowned for its simplicity, reliability, and computational efficiency [32], the Swanepoel method operates in the order of a few seconds on standard computers, making it ideal for rapid mass characterization of

Optics EXPRESS

samples. Additionally, it is considered a "model-free" method, meaning that it does not rely on pre-established optical dispersion models for $n(\lambda)$ and $k(\lambda)$.

This method analyzes the interference patterns created by a quasi-monochromatic beam as it passes through a thin film, where the patterns result from the superposition of multiple internal reflections within the film (see Fig. 1(b)). For the desired etalon (Fabry-Perot) effect to manifest prominently within the thin film, the coherence length of the beam must exceed the film thickness (typically on the micrometer scale), denoted d. This ensures that multiple internal reflections within the film lead to significant constructive and destructive interference, depending on the wavelength. Consequently, the transmission spectrum $T(\lambda)$ exhibits characteristic sinusoidal oscillations with distinct peaks and valleys, as illustrated in Fig. 1(c). The Swanepoel method exploits these spectral oscillations to accurately determine the film properties. Note that in order to prevent the substrate from generating its own etalon effects, the coherence length must be set shorter than the substrate thickness (typically on the millimeter scale), denoted d_s. As the coherence length increases with wavelength, it may eventually exceed the substrate thickness

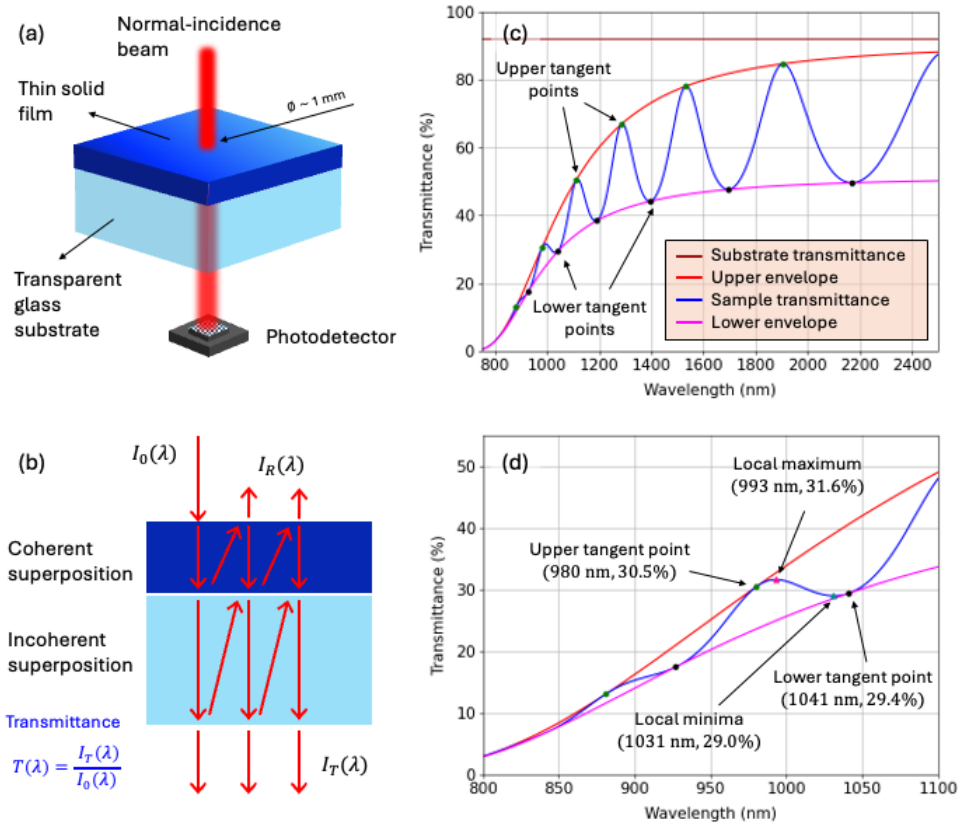


Fig. 1. (a) Schematic of the sample geometry, comprising a thin layer deposited on a glass substrate. (b) Multiple internal reflections within the thin film and the substrate. The total transmittance is measured sequentially throughout different wavelengths. (c) Simulated transmission spectra for the full sample and for the substrate alone. The ground-truth upper and lower envelopes, along with their tangent points, are indicated. (d) Magnified view of the strongly absorbing spectral region. The upper and lower tangent points are sometimes not associated with a nearby local extremum (first two on the left), or occur at positions significantly far from the local extrema (last two on the right).

Optics EXPRESS

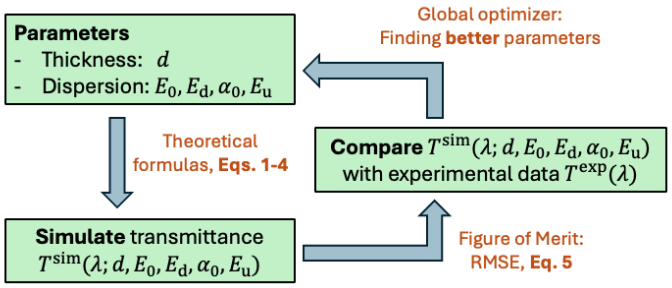


Fig. 2. Random initial guesses for the film parameters (such as thickness and the coefficients of the optical dispersion model) are selected. A theoretical transmittance spectrum is calculated from these parameters via Eq. (1). The simulated spectrum is then compared to the experimental spectrum, and the residual error is quantified using the cost function (RMSE) defined in Eq. (5). A global optimization algorithm iteratively adjusts the parameters to minimize this residual error. This process repeats until the optimal parameters that yield the best fit between the simulated and experimental spectra are found.

at longer wavelengths. This can lead to very high-frequency oscillations [33], causing aliasing when the oscillation frequency surpasses the spectral sampling rate used in the experiment. Such aliasing manifests as characteristic noise at the spectrum's end if the experiment is not carefully calibrated. This condition ensures that any multiple reflections within the substrate do not contribute to coherent interference patterns, resulting instead in an incoherent superposition of the beams. The exact value of d_s is therefore not relevant for the characterization of the sample.

Since its inception, the Swanepoel method has served as a key computational method for the analysis of thin-film optical analysis, inspiring numerous enhancements that have significantly broadened its applicability. For instance, shortly after introducing his original algorithm, Swanepoel himself extended the methodology in 1984 [34], enabling the analysis of films with tilted planar-specular surfaces. The algorithm can then apply to samples with non-uniform thickness, generally characterized by a wedge Δd. Recognizing the limitations of spectrophotometric measurements for accurate film analysis, Swanepoel proposed an improved method in 1985 [35]. This approach involved acquiring transmission spectra at two different angles of incidence: one at normal incidence and the other at an oblique angle. By analyzing the shift in the spectral domain between these two measurements, the method enabled the direct determination of both the film thickness d and refractive index n without relying on the absolute transmittance values. In 1986, Kushev *et al.* generalized the envelope method to the field of reflectometry [36], enabling the determination of thin-film optical properties from normal-incidence reflectance measurements. In 1989, another work by Swanepoel now accounted for the substrate absorption [37]. In 1995, Nowak [38] investigated the effects of realistic band-limited incident beams with either linear or Gaussian spectral profiles, further refining the accuracy of the method. Later, Wu *et al.* (2008) [39] extended the method to analyze inhomogeneous films with a linearly graded refractive index from the substrate interface to the film surface. Jin *et al.* contributed two very significant advancements in 2017. First, they analyzed the spectral regions in which the film presents strong absorption [40], where the original Swanepoel method produced substantially less accurate solutions. Then, they expanding the algorithm to determine the refractive index n and extinction coefficient k at arbitrary wavelengths, not just at the mentioned tangent points [41].

In addition to the Swanepoel method, the *inverse synthesis* approach serves as a powerful alternative for the optical characterization of thin films [42–45]. This method involves fitting experimentally measured transmission spectra with a simulated transmission curve, which is

Optics EXPRESS

derived from pre-defined dispersion models for the refractive index $n(\lambda)$ and the extinction coefficient $k(\lambda)$. One of the key advantages of the inverse synthesis approach is its ability to provide precise optical characterization over a continuous broad spectral range [46]. Furthermore, this method allows for the modeling of more complex physical scenarios, including surface roughness, refractive index gradients, and non-uniform film thickness with specific geometries. The conventional Swanepoel method approximates these realistic films as a simple, idealized homogeneous layers. Neglecting these film imperfections leads to correlated effects on the spectral envelopes, making it impossible to distinguish such features based on spectro photometric measurements alone. Consequently, the Swanepoel method is primarily useful as a first-order approximation for optical characterization [46,47]. Envelope-based characterization can serve as a preliminary estimate for subsequent refinement using inverse synthesis.

Despite its advantages, it should be noted that the inverse synthesis approach can be computationally intensive. Additionally, solving the inverse problem does not always guarantee physically meaningful solutions, as the optimization algorithm may converge to incorrect local minima, leading to non-physical parameter estimations (this problem is further discussed in the next section). Given these challenges, it is often advisable to use the simpler Swanepoel method as a complementary tool for validation and cross-checking of results, a practice commonly reported in the literature [47,48]. Implementing the inverse synthesis approach is non-trivial and demands careful parameter selection. This reverse engineering approach relies on an appropriate dispersion formula that accurately describes the refractive index and absorption behavior of the film material. In some cases, determining a suitable model requires a detailed understanding of the material's electronic transitions to correctly incorporate contributions from different optical oscillators. A variety of dispersion models are available, ranging from the simple empirical Cauchy model (suitable for transparent materials such as glass), to more sophisticated physically-motivated models, like the Tauc-Lorentz (TL) or Cody-Lorentz (CL) models [49], which account for absorption. The development of more advanced dispersion models remains an active area of research, with recent efforts focusing on models such as the Analytical Tauc/Cody-Lorentz Urbach (ATLU or ACLU) model [50–52] or the Universal Dispersion Model (UDM) [53–56], which provides broad applicability across different material classes and spectral ranges.

Besides the envelope method and the inverse synthesis, further computational approaches are emerging. For instance, there is a Deep Learning architecture that directly predicts a film properties from transmission data [57]. Another recent technique employs a digital twin [58] to numerically simulate wave propagation through the spectrophotometer.

Envelope detection algorithms: The Swanepoel method assumes precise knowledge of both the upper and lower envelopes of the transmission spectrum (refer to Fig. 1(b)). In practice, accurately identifying these envelopes is a significant challenge on its own. The accuracy of the Swanepoel method is highly dependent on the precise determination of these envelopes, as any discrepancies in their construction propagate through the entire algebraic procedure, ultimately affecting the reliability of the film characterization. In 1991, Marjorie McClain *et al.* [59] addressed this problem by introducing a robust iterative algorithm for envelope construction. This seminal work has since established the McClain algorithm as the standard approach, extensively utilized in the literature [60–62]. The McClain algorithm is both efficient and reasonably accurate in practical applications. It determines the envelopes using B-spline interpolation of the mentioned tangent points, which are seen in Fig. 1(c). As anticipated, the accuracy of this interpolation-based method improves with an increasing number of interpolation nodes, requiring at least four spectral oscillations with its four associated tangent points to produce reliable results. Beyond the original McClain algorithm, several other interpolation-based methodologies have been proposed to enhance envelope detection [63–66].

Alternative approaches have been developed to address spectra with limited number of oscillations, sometimes displaying only two or three tangent points. A common strategy in

Optics EXPRESS

such scenarios involves fitting the envelopes by connecting local extrema (maxima for the upper envelope and minima for the lower envelope) using predefined exponential [67,68] or parabolic functions [69]. However, it should be mentioned that, although the tangent points typically lie near the extrema of the transmission spectrum, they do *not* coincide precisely. Indeed, observe that the film absorption induces a decay in the transmittance curve as wavelengths decrease and approximates the optical band gap, causing the tangent points to shift slightly away from the extrema, as seen in Fig. 1(d). In the regions of strong film absorption (where the transmission spectrum remains low) the tangent points may not correspond to any local minimum or maximum at all, as illustrated by the first lower and upper tangent points of the simulated spectrum, in Fig. 1(d). Consequently, the mentioned parabolic and exponential fits often lead to noticeable errors in the constructed envelopes. A recently proposed deep learning–based method [70] developed by our team shows promise in accurately determining envelopes for transmission spectra, even in these challenging scenarios with as few as two or three tangent points. However, this approach has so far been validated only with simulated data and not with real, noisy experimental measurements.

Enhancing the accuracy of envelope computation remains a significant and ongoing challenge in the field. In the present work, we propose a novel interpolation-based algorithm for the precise determination of Swanepoel envelopes. Our approach integrates the physical properties of the Swanepoel envelopes into a global optimization framework, which is then efficiently solved using an advanced optimizer. We validated our method using fifty computer-generated transmission spectra, achieving a root-mean-square error (RMSE) of less than 0.10% for the upper envelope and below 0.06% for the lower envelope. These results demonstrate a significant enhancement in accuracy compared to existing methods, reducing errors by more than half with respect to the standard McClain algorithm, as detailed in the subsequent comparison section. While our proposed method is more computationally expensive than the existing algorithms, it still performs in a reasonable timeframe and runs in less than a minute using standard computer hardware.

Furthermore, we have integrated our innovative envelope construction algorithm with an automated adaptation of the original Swanepoel method within a user-friendly Python package named `swanpy`. This open-source software is publicly accessible at [71]. Note that `swanpy` does not only includes our novel envelope construction algorithm but also incorporates additional standard envelope detection techniques for comparative analysis. Our automated and efficient implementation of the Swanepoel method facilitates the comprehensive optical characterization of thin films. It is worth noting that the present work demonstrates the effectiveness of `swanpy` in practical applications by fully characterizing two real amorphous silicon (a-Si) samples, which were previously analyzed by our team [48] and used here as a benchmark.

2. Thin film transmission equation and inverse-synthesis challenge

As discussed earlier, the inverse synthesis method requires a simulator to reproduce the transmission curve, which is then fitted to experimental data. To develop such a simulator, we begin with the theoretical expression for normal-incidence transmittance, derived from the Fresnel equations [72]. Following extensive derivations in [33], the final formula relates the wavelength λ and the film's optical properties (n, k, d) to the transmittance. Assuming a uniform, isotropic, and homogeneous film deposited on a transparent substrate with a known refractive index n_s, the resulting expression is:

$$T^{\text{sim}}(\lambda; n, k, d) = \frac{A'x}{B' + x(C'_1 \sin\varphi - C'_2 \cos\varphi) + D'x^2}, \tag{1}$$

where

$$\alpha = 4\pi k/\lambda, \tag{2a}$$

Optics EXPRESS

$$x = e^{-\alpha d}, \tag{2b}$$

$$\varphi = 4\pi n d/\lambda, \tag{2c}$$

$$A' = 16(n^2 + k^2)n_s, \tag{2d}$$

$$B' = \left((n+1)^2 + k^2\right)\left((n+1)(n+n_s^2) + k^2\right), \tag{2e}$$

$$C_1' = 2k\left(2(n^2 + k^2 - n_s^2) + (n^2 + k^2 - 1)(n_s^2 + 1)\right), \tag{2f}$$

$$C_2' = 2(n^2 + k^2 - 1)(n^2 + k^2 - n_s^2) - 4k^2(n_s^2 + 1), \tag{2g}$$

$$D' = \left((n-1)(n-n_s^2) + k^2\right)\left((n-1)^2 + k^2\right). \tag{2h}$$

Observe that the refractive index of the substrate, n_s, is known because it can be computed beforehand from the transmission of the substrate alone, T_s, using the equation [33]:

$$n_s = 1/T_s + \sqrt{1/T_s^2 - 1}. \tag{3}$$

It should also be emphasized that α (1/cm) in Eq. (2a) corresponds to the absorption coefficient. Additionally, the term x in Eq. (2b) denotes the a fraction of the transmitted intensity: this parameters is calculated from the Lambert-Beer law [72] and ranges from 0 to 1, expressing the amount of light that passes through the film in one single pass (not accounting for multiple round trips of the beam within the film). Lastly, the two trigonometric functions in the denominator of Eq. (1) depend on the phase φ and account for the Fabry-Perot thin-film interferences, corresponding to the low-frequency oscillations noticeable in the transmission spectrum.

One could naively develop a least-squares regression program to fit the experimental transmission spectrum $T(\lambda)$ to the theoretical model $T^{\text{sim}}(\lambda; n(\lambda), k(\lambda), d)$, thereby determining the film's optical and geometrical properties $n(\lambda)$, $k(\lambda)$, and d. However, n and k are intricate wavelength-dependent functions and not simple constants. Multiple combinations of n and k can produce the same theoretical transmission spectrum, making this fitting problem *ill-posed* in nature. As Kushev and Zheleva [36] realized in 1986, "the system is satisfied by many solutions and it is difficult to identify the real physical one".

The *inverse synthesis* method takes this fitting idea a step further and eases the problem by assuming some pre-defined dispersion models for the optical functions $n(\lambda)$ and $k(\lambda)$. Consequently, these complicated optical functions are expressed in terms of just a few real coefficients. For instance, one can employ the simple Wemple-DiDomenico (WDD) dispersion equation [73] for n and the Urbach rule [74] for the absorption coefficient α (the extinction coefficient k can then be derived using Eq. (2a)). We then have the following formulas:

$$n(E; E_0, E_\text{d}) = \sqrt{\frac{E_0 E_\text{d}}{E_0^2 - E^2} + 1}, \tag{4a}$$

$$\alpha(E; \alpha_0, E_\text{u}) = \alpha_0 \exp\left(\frac{E}{E_\text{u}}\right). \tag{4b}$$

The parameter E_0 (eV) represents the oscillator energy in a single-oscillator electron model. In practice, this number quantifies an average energy gap of the different electronic transitions and provides a good approximation of the optical bandgap energy, $E_\text{g} \approx E_0/2$ [75,76]. E_d (eV) is the dispersion energy, which quantifies the strength of interband optical transitions and provides an extra degree of freedom to account for the refractive index value as the photon energy approaches zero $E \to 0$. The parameter α_0 (1/cm) defines the absorption coefficient in the limit of zero photon energy. The Urbach energy, denoted as E_u (eV), characterizes the exponential decay of the absorption coefficient with decreasing photon energy below the bandgap, indicating the

Optics EXPRESS

degree of structural disorder in amorphous materials responsible for sub-bandgap absorption. Please note that Eqs. (4a)–(4b) can be similarly expressed as functions of wavelength using the Planck-Einstein relation $E = hc/\lambda$, where h is Planck's constant and c is the speed of light in vacuum.

The combined WDD-Urbach model offers a foundational estimate of the electronic transitions in thin-film materials. This model is primarily applicable to amorphous materials with two main energy levels, encompassing a single dominant electronic transition between the valence and conduction bands, which defines the bandgap energy. However, it disregards weaker transitions that may play a significant role in crystalline materials. Furthermore, this dispersion model is limited to specific spectral regions, particularly for photon energies that are well below the optical bandgap but remain sufficiently separated from phonon resonances in the near-infrared range. In the simulated example illustrated in Fig. 1, we used the following parameter values: $E_0 = 4.28$ eV, $E_\mathrm{d} = 30.45$ eV, $\alpha_0 = 269.46$ mm^{-1}, $E_\mathrm{u} = 229.18$ meV, and $d = 1323$ nm.

Employing more precise models that are consistent with the Kramers-Kronig relations between n and k increases computational complexity considerably. This complexity is particularly evident when utilizing various modifications and adaptations of the Tauc-Lorentz-Urbach (TLU) [48–50,77] and Cody-Lorentz-Urbach (CLU) [49,51,78] models, which are valid across the entire spectral range. These advanced models, enhanced with numerous refinements, necessitate extensive computations and introduce additional subtle and intricate variables into the simulator.

Regardless of the optical dispersion model chosen, the inverse synthesis approach enables the simplification of the transmittance formula $T(\lambda; n(\lambda), k(\lambda), d)$ from Eq. (1) in terms of only a few input coefficients. In our case, the WDD-Urbach model allows us to rewrite the simulated transmission curve as a function of $(E_0, E_\mathrm{d}, \alpha_0, E_\mathrm{u}, d) \in \mathbb{R}^5$. With these scalar values, we can establish the following least-squares optimization problem (outlined in Fig. 2):

$$\begin{aligned} &\text{minimize} \quad C(E_0, E_\mathrm{d}, \alpha_0, E_\mathrm{u}, d) = \mathrm{RMSE}(T, T^\mathrm{sim}) = \sqrt{\frac{\sum_{i=0}^{N} \left[T(\lambda_i) - T^\mathrm{sim}(\lambda_i; E_0, E_\mathrm{d}, \alpha_0, E_\mathrm{u}, d)\right]^2}{N}}, \\ &\text{subject to} \quad \begin{cases} E_0 \in [a_1, b_1], & E_\mathrm{d} \in [a_2, b_2], \\ \alpha_0 \in [a_3, b_3], & E_\mathrm{u} \in [a_4, b_4], \\ d \in [a_5, b_5]. \end{cases} \end{aligned} \tag{5}$$

The cost function C quantifies the discrepancy between the predicted and experimental spectra across the discrete wavelengths within the spectral region of interest (ROI). Achieving cost values below 1-1.5% typically indicates a good fit between the simulated and measured data [48,79]. However, the acceptable threshold for the cost function depends on the spectral range length and the specific characteristics or noise level of the measurements. Note that in Eq. (5), the box constraints $[a_i, b_i]$ define the acceptable ranges for the parameters, which vary depending on the specific thin-film material under investigation.

Although this inverse synthesis approach is a popular choice for optical characterization, it is not without limitations. For instance, there is the crucial task of setting feasible constraint ranges for a_i and b_i, as the computational effort increases notably when these ranges are broadened. Furthermore, the inverse problem is inherently non-convex in nature, marked by numerous local minima and maxima, and necessitating the use of sophisticated global optimization algorithms. These global optimizers are often affected by the curse of dimensionality, resulting in substantially increased computational costs as the number of variables grows. Additionally, in practical scenarios with noisy data and approximated simulation models, these algorithms can still produce solutions that are mathematically acceptable (satisfying constraints and exhibiting low cost values) but physically inaccurate, corresponding to local minima rather than the global optimum.

Optics EXPRESS

To mitigate the risk of converging to suboptimal local minima, it is recommended to execute these optimization algorithms multiple times with different initial points or random seeds and to compare the resulting solutions. This approach enhances the likelihood of identifying the most accurate and reliable characterization of the system.

The runtime of the inverse synthesis method is influenced by several factors, including the particular dispersion model employed and its number of variables, the choice of the global optimizer and its hyperparameters (such as the number of iterations or initial seeds), the range of the box constraints, and the number of times the optimization is executed to corroborate results. Consequently, solving the inverse problem described by Eq. (5) can become a computationally intensive task, sometimes requiring hours of manual fine-tuning and computation.

For a later comparison of our improved Swanepoel method, we use now the inverse synthesis method to characterize two real spectra. Specifically, two *a*-Si samples were prepared using radio-frequency magnetron sputtering (RFMS) on top of a transparent Corning Eagle XG glass substrate. The target p-type silicon had a 5N purity and a density of 2.32 g/cm^3. During thin-film deposition, the RFMS chamber was maintained at room temperature (25 °C) with an RF power of 525 W. The deposition rates were 1.269 nm/s for sample #1 and 1.339 nm/s for sample #2. The chamber pressures were 4.4 Pa and 3.2 Pa, and the argon gas flow rates were 70 sccm and 50 sccm for samples #1 and #2, respectively.

Transmission measurements of both the substrate alone and the full sample were collected using an Agilent Cary 5000 double-beam spectrophotometer, covering the UV-VIS-NIR range from 300 to 2500 nm. The initial spectral range (up to 700 nm) was cropped out to avoid the interval where the substrate exhibits considerable absorption and where the thin film shows very strong absorption (leading to a near-zero transmission), which provides no useful information for characterization. The fitting problem was then solved using the Simulated Dual Annealing algorithm, an efficient global optimizer available in the Python `scipy` package [80]. Figure 3 illustrates the agreement between the experimental and simulated spectra, with root mean square errors (RMSE) of 0.85% for sample #1 and 0.98% for sample #2. The bottom panel of the figure displays the residual disagreement or fitting error, defined as $T^{\text{exp}} - T^{\text{sim}}$. Notably, in the NIR region beyond 2100 nm, where the substrate exhibits slight absorption, a stronger disagreement is observed in Fig. 3(a).

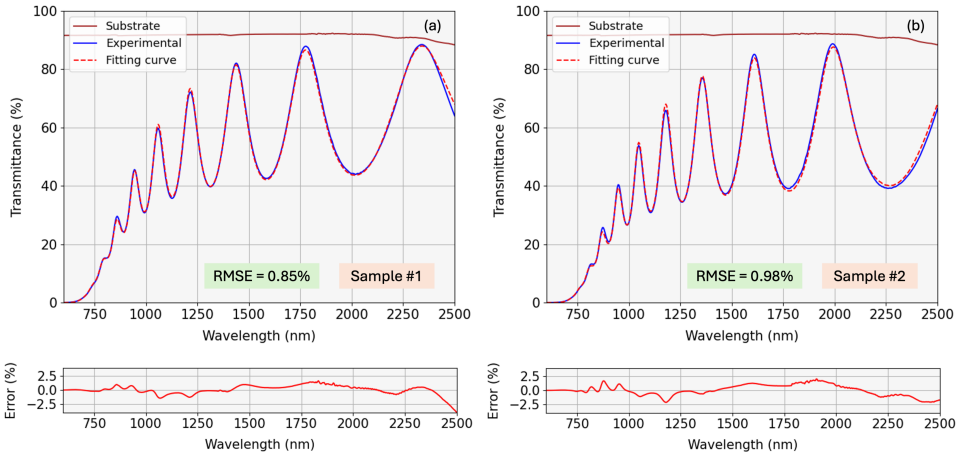


Fig. 3. Comparison of experimental transmission measurements with simulated transmission curves for (a) sample #1 and (b) sample #2 of amorphous silicon, obtained using the inverse synthesis method. The bottom panels illustrate the residual differences or error between the experimental and simulated data, defined as $T^{\text{exp}} - T^{\text{sim}}$.

Optics EXPRESS

The optimal parameters obtained from the inverse synthesis method for samples #1 and #2 are summarized in Table 1. Initially, the points for the optimization were randomly chosen within the specified bounds for each parameter. In this particular case, the optimization process required only a few minutes of computation time and manual adjustments of the bounds, thanks to the relatively low dimensionality of the simplistic models for n and k employed here for illustrative purposes.

Table 1. Optimized parameters for amorphous silicon samples obtained from the inverse synthesis method. The initial bounds for each parameter are also provided.

Parameter	Unit	Lower Bound	Upper Bound	Sample #1	Sample #2
Thickness d	nm	500	1500	1117	1160
Oscillator energy E_0	eV	3.2	5.0	3.22	3.21
Dispersion energy E_d	eV	25	35	27.96	33.28
Absorption coefficient α_0	cm^{-1}	0.1	0.5	0.225	0.186
Urbach energy E_u	eV	0.1	0.3	0.247	0.234

3. Automated Swanepoel method

As previously noted, the Swanepoel method provides a more straightforward alternative to the inverse synthesis approach. It relies on the principles of Fabry-Perot interference and employs the simple algebraic interference formula to perform the optical characterization. Although the method's approximations can reduce the precision of the estimated film properties, it offers several key advantages: it requires far less computational effort, imposes no dispersion assumptions, and avoids multiple non-physical solutions. In other words, instead of encountering the ambiguity often faced with inverse synthesis methods, the Swanepoel approach yields a unique, physically meaningful set of values for n, k, and d.

Our automated program is based on the original Swanepoel algorithm from 1983 [28,81], designed specifically for plane-parallel thin films of uniform thickness, composed of isotropic and homogeneous materials. As previously discussed, numerous adaptations of this algorithm have been proposed to handle more complex scenarios [34,36,38–41], and these enhancements could potentially be integrated into our software framework in the future.

In spectral regions where the sample presents medium-to-weak optical absorption, the condition $n^2 \gg k^2$ holds. These spectral regions, frequently examined in transmission spectroscopy studies, correspond to photon energies below the optical bandgap. Under this circumstance, Eq. (1) can be simplified as follows:

$$T^{\mathrm{sim}}(\lambda; n, k, d) = \frac{Ax}{B - Cx\cos\varphi + Dx^2}, \tag{6}$$

Observe that the fraction of transmitted intensity x and the phase ϕ were previously defined in Eq. (2b) and (2c), respectively. Additionally, we use the following new expressions:

$$\begin{aligned} A &= 16n^2 n_s, \\ B &= (n+1)^3(n+n_s^2), \\ C &= 2(n^2-1)(n^2-n_s^2), \\ D &= (n-1)^3(n-n_s^2). \end{aligned} \tag{7}$$

In contrast with the more accurate transmittance expression from Eq. (1), the formula for T^{sim} given in Eq. (6) now only comprises a single sinusoidal function. Therefore, we can find the two envelopes of the oscillating transmission curve by assigning $\cos(\varphi) = 1$ for the upper

Optics EXPRESS

envelope T_M^{sim}, and $\cos(\varphi) = -1$ for the lower envelope T_m^{sim}. These envelopes are then expressed as follows:

$$T_M^{\text{sim}}(\lambda; n, k, d) = \frac{Ax}{B - Cx + Dx^2}, \tag{8a}$$

$$T_m^{\text{sim}}(\lambda; n, k, d) = \frac{Ax}{B + Cx + Dx^2}. \tag{8b}$$

The intersection points between the simulated transmission spectrum T^{sim} and its upper envelope T_M^{sim} are identified as the upper tangent points, which are represented by λ^{M}, as shown in Fig. 1(b). Similarly, λ^{m} denotes the lower tangent points, which are associated with the intersections of T^{sim} with its lower envelope T_m^{sim}. Due to the sinusoidal characteristic of Fabry-Perot oscillations, these upper and lower tangent points occur in an alternating pattern. The sorted sequence of these tangent points is expressed here as λ^{tan}.

While determining the simulated envelopes of a simulated transmission curve is straightforward, following their definition from Eq. (8) (as done for the initial Fig. 1), identifying the Swanepoel envelopes of an *experimental* curve poses a significant challenge. The Swanepoel method assumes that the true envelopes, T_M and T_m , of a measured transmission spectrum T have already been (somehow) accurately determined. Based on this assumption, the optical properties n and k are extracted using a series of physically meaningful equations, evaluated exclusively at the tangent points. Below, we detail our automated step-by-step procedure for implementing the Swanepoel method, which is summarized in Fig. 4.

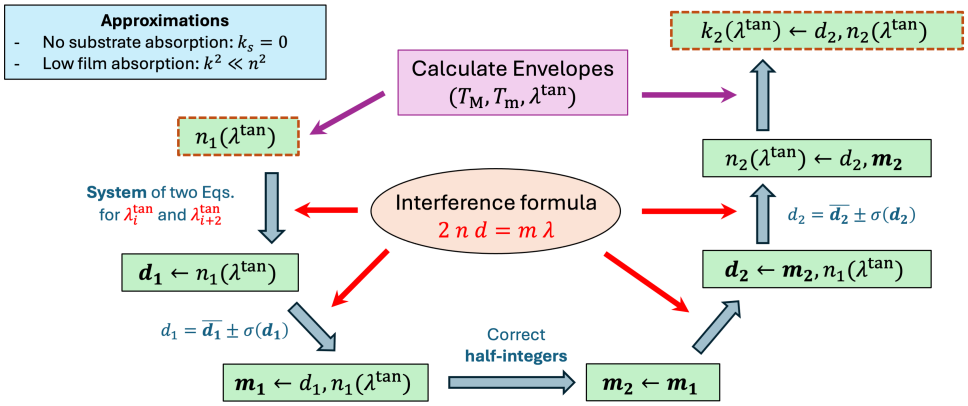


Fig. 4. Summary of the Swanepoel method: the steps are marked in green, starting at the top left. (1) After computing the transmission envelopes, initial estimates of the refractive index n_1 are determined at the tangent wavelengths λ^{tan}. (2) A system of two equations (based on the interference formula) is solved at each pair of adjacent tangents point to estimate the film thickness, resulting in a set of possible thickness $\mathbf{d_1}$. The expected thickness value is calculated as $d_1 = \text{mean}(\mathbf{d_1}) \pm \text{std}(\mathbf{d_1})$. (3) The interference formula is then applied again to compute the interference orders $\mathbf{m_1}$. (4) These calculated decimal values should theoretically be half-integers, so they are updated to the nearest corrected values $\mathbf{m_2}$. (5) With these corrected interference orders, a more precise thickness estimate $d_2 = \text{mean}(\mathbf{d_2}) \pm \text{std}(\mathbf{d_2})$ is obtained using the interference formula. (6) This refined thickness allows for updated refractive index values n_2 at the tangent points. (7) Finally, an accurate extinction coefficient k_2 is computed at the tangent points using the precise d_2, the updated refractive index n_2, and information from the envelopes.

Optics EXPRESS

3.1. Preliminary estimation of n_1 and d_1

In this preliminary step, we carry out a rough estimation of the refractive index (n_1) and film thickness (d_1). One can obtain a formula for the refractive index using Eq. (6) and Eqs. (8a)–(8b), leading to

$$\begin{aligned} n_1 &= \sqrt{N + \sqrt{N^2 - n_s^2}}, \text{ where} \\ N &= 2n_s \frac{T_M - T_m}{T_M T_m} + \frac{n_s^2 + 1}{2} \end{aligned} \tag{9}$$

Equation (9) is then evaluated at each tangent point, yielding the series of values $n_1(\lambda^{\tan})$. Table 2 lists these computed values $n_1(\lambda^{\tan})$ corresponding to the spectra illustrated in Fig. 1(b). Subsequently, we utilize the fundamental Fabry-Perot interference [82] equation:

$$2n(\lambda)d = m\lambda. \tag{10}$$

This well-established relation holds only at the *tangent* points ($\lambda = \lambda^{\tan}$), which explicitly denote the transition between constructive and destructive interferences, or vice-versa. The variable m symbolizes the interference order, a number in the set $\mathbb{N}/2 = \{1/2, 1, 3/2, 2, 5/2, \ldots\}$ and therefore referred to as a "half-integer." Note that the successive tangent points, arranged from longer to shorter wavelengths, correspond to consecutive interference orders. For instance, Table 2 lists the values of m that range from 3.0 to 10.0 for sample #1, with increments of 0.5.

Two adjacent upper tangent points (or two adjacent lower points), denoted as $\lambda_i^{\tan}$ and $\lambda_{i+2}^{\tan}$, have orders of interference m and $m + 1$, respectively. Therefore, we can define the following system of equations:

$$\begin{cases} 2n_1(\lambda_i^{\tan})d_1 = m\lambda_i^{\tan} \\ 2n_1(\lambda_{i+2}^{\tan})d_1 = (m+1)\lambda_{i+2}^{\tan} \end{cases} \tag{11}$$

Knowing now $\lambda_i^{\tan}$ and $n_1(\lambda_i^{\tan})$ for each tangent point i, we can solve Eq. (11) for the unknown variable d_1. The equation can be solved to find the d_1 values for the different tangent points, except for the two greater ones (as the system needs the points i and $i + 2$). The set of values $\mathbf{d_1}$ represents the thickness estimations using data from the multiple tangent points (see Table 2). Ideally, each of these d_1 values should be identical. In practice, the thickness is approximated as $d_1 = \text{mean}(\mathbf{d_1}) \pm \text{std}(\mathbf{d_1})$.

Sometimes, it is advisable to exclude the elements of $\mathbf{d_1}$ corresponding to the shorter wavelengths if they clearly differ from the the mean value, as they are often not very consistent with the other values (see the marked numbers on the Table 2). This discrepancy arises when there exists a strong absorption at shorter wavelengths, as the Swanepoel approximation ($n \gg k$) becomes less accurate.

3.2. Refining the values of n_2 and d_2

The previous estimates are highly sensitive to noise from the experimental transmission measurements and errors in the two corresponding envelopes. Therefore, it is important to go through a second refinement step to find more suitable values of n_2 and d_2. First, note that we can now calculate the "inexact" half-integers (denoted by $\mathbf{m_1}$) by inserting the predicted rough values $n_1(\lambda^{\tan})$ and d_1 in Eq. (10), yielding $\mathbf{m_1} = 2n_1(\lambda^{\tan})d_1/\lambda^{\tan}$. The set of approximated values $\mathbf{m_1}$ are shown in the 6th column of Table 2.

We know that $\mathbf{m_1}$ should theoretically be half-integers, so we can improve the found values. Indeed, one will now search for the sequence of consecutive half-integers $\mathbf{m_2}$ that best match the approximated data $\mathbf{m_1}$. This process can be automated by formulating a fitting problem and employing the direct search method, an effective global optimization technique well-suited for this straightforward, low-dimensional scenario. Specifically, we identify the optimal sequence

Optics EXPRESS

Table 2. Results of the Swanepoel method applied to the transmission spectra of Sample #1 and Sample #2. The estimated thicknesses are provided along with their standard deviations and relative errors compared to the thicknesses obtained from the inverse synthesis method. For Sample #1, d_1 = 1099.32 ± 35.77 nm (relative error = 3.25%) and d_2 = 1110.18 ± 7.22 nm (relative error = 0.65%). For Sample #2, d_1 = 1167.28 ± 62.92 nm (relative error = 5.39%) and d_2 = 1163.88 ± 10.52 nm (relative error = 0.90%). The last two data points in each sample are crossed out due to unreliable calculations at shorter wavelengths.

Tan (nm)	T_m (%)	T_M (%)	n_1	d_1 (nm)	Half int inexact	Half int exact	d_2 (nm)	n_2	k_2 ($\times 10^3$)	α_2 ($\times 10^3$ cm^{-1})	x_2
Sample #1											
2340.0	44.35	88.46	3.2049	–	3.0113	3.0	1095.19	3.1616	2.9	0.1550	0.9829
2020.0	43.94	88.28	3.1535	–	3.4324	3.5	1120.97	3.1842	4.2	0.2614	0.9714
1776.0	43.35	87.90	3.1818	1185.00	3.9390	4.0	1116.34	3.1995	4.0	0.2836	0.9690
1588.0	42.56	85.61	3.1940	1110.70	4.4222	4.5	1118.68	3.2184	5.6	0.4458	0.9517
1436.0	41.28	82.01	3.2289	1094.23	4.9437	5.0	1111.85	3.2337	7.9	0.6948	0.9258
1316.0	39.72	77.51	3.2443	1101.41	5.4203	5.5	1115.50	3.2598	11.0	1.0545	0.8895
1216.0	37.90	72.17	3.2718	1130.93	5.9157	6.0	1114.98	3.2859	14.5	1.4990	0.8467
1128.0	35.72	65.99	3.3037	1078.69	6.4394	6.5	1109.67	3.3022	18.6	2.0713	0.7946
1056.0	33.39	59.50	3.3333	1073.15	6.9401	7.0	1108.81	3.3292	23.0	2.7408	0.7377
996.0	30.84	52.76	3.3677	1105.09	7.4342	7.5	1109.06	3.3643	28.0	3.5269	0.6760
944.0	27.89	45.57	3.4117	1092.79	7.9461	8.0	1106.78	3.4012	33.9	4.5095	0.6061
896.0	24.33	37.19	3.4421	1086.14	8.4463	8.5	1106.31	3.4301	42.3	5.9310	0.5177
856.0	20.29	29.20	3.5074	1034.42	9.0088	9.0	1098.25	3.4697	52.3	7.6742	0.4266
820.0	15.99	21.16	3.5336	~~1068.99~~	9.4747	9.5	–	–	–	–	–
788.0	11.62	14.25	3.5865	~~1101.34~~	10.0070	10.0	–	–	–	–	–
Sample #2											
2260.0	39.13	89.72	3.4974	–	3.6128	3.5	1130.84	3.3981	1.3	0.0706	0.9918
1992.0	39.12	88.71	3.4246	–	4.0136	4.0	1163.33	3.4230	3.2	0.2050	0.9764
1776.0	39.09	87.20	3.4086	1345.01	4.4806	4.5	1172.33	3.4333	4.3	0.3011	0.9656
1608.0	38.38	85.11	3.4256	1216.15	4.9734	5.0	1173.53	3.4540	5.6	0.4359	0.9505
1472.0	37.27	81.60	3.4566	1165.49	5.4822	5.5	1171.08	3.4780	7.8	0.6642	0.9256
1356.0	35.93	76.99	3.4765	1153.44	5.9854	6.0	1170.13	3.4952	10.8	0.9974	0.8904
1260.0	34.40	71.62	3.5049	1153.61	6.4940	6.5	1168.36	3.5184	14.1	1.4067	0.8490
1180.0	32.75	65.89	3.5296	1170.04	6.9830	7.0	1170.12	3.5485	17.7	1.8860	0.8029
1108.0	30.85	59.89	3.5632	1151.50	7.5077	7.5	1166.08	3.5699	21.6	2.4504	0.7519
1048.0	28.89	53.84	3.5932	1142.88	8.0044	8.0	1166.64	3.6017	25.7	3.0864	0.6982
992.0	26.54	46.93	3.6257	1138.98	8.5326	8.5	1162.82	3.6224	31.1	3.9394	0.6322
948.0	24.05	40.39	3.6679	1135.25	9.0326	9.0	1163.07	3.6653	36.8	4.8776	0.5668
904.0	20.81	32.28	3.6903	1170.02	9.5302	9.5	1163.58	3.6894	45.8	6.3617	0.4769
868.0	17.24	24.95	3.7659	~~1065.01~~	10.1286	10.0	–	–	–	–	–
836.0	13.55	18.09	3.7984	~~1083.89~~	10.6072	10.5	–	–	–	–	–

Optics EXPRESS

of consecutive half-integers that minimizes the absolute error distance relative to our set of approximate interference orders m_1. The refined values $\mathbf{m_2}$ are presented in the seventh column of Table 2.

Setting now $n_1(\lambda^{\tan})$ and the *exact* values of $\mathbf{m_2}$ into Eq. (10), we can determine a new array $\mathbf{d_2}$ with more accurate film-thickness estimates: $\mathbf{d_2} = \mathbf{m_2}\lambda^{\tan}/2n_1(\lambda^{\tan})$. The corrected film thickness is then computed as $d_2 = \text{mean}(\mathbf{d_2}) \pm \text{std}(\mathbf{d_2})$. These values are shown in the 8th column of Table 2. In the two example shown in the table, one can see noticeable improvements from d_1 to d_2, reducing the uncertainty of the thickness value by an order of magnitude.

Finally, one can employ the interference formula once again to compute the corrected refractive index $n_2(\lambda^{\tan})$. Note that the known values that we introduce in the interference formula are the exact set of values $\mathbf{m_2}$ and the highly accurate thickness d_2. In particular, we now compute $n_2(\lambda^{\tan}) = \mathbf{m_2}\lambda^{\tan}/2d_2$.

3.3. Finding k_2

With the refined values of the refractive index $n_2(\lambda^{\tan})$ and thickness d_2, we now aim to find precise values of the extinction coefficient $k_2(\lambda^{\tan})$ at each tangent point. Observe that since the extinction coefficient k, the absorption coefficient α, and the variable x are directly related through Eqs. (2a)–2b, it is sufficient to estimate any one of these quantities. We will then analyze x.

The variables (A, B, C, D) from Eq. (7) depend only on n and d, and can now be accurately calculated using the refined values $n_2(\lambda^{\tan})$ and d_2. Considering that the envelopes T_M and T_m were (somehow) previously calculated, we can now solve either Eqs. (8a) or (8b) for $x_2(\lambda^{\tan})$ at each wavelength $\lambda^{\tan}$. It is important to note that these equations are quadratic, resulting in two possible ambiguous results for x_2. However, it must be remarked again that the parameter x_2 represents a fraction of transmitted intensity: the beam intensity transmitted in a single pass through the thin film, neglecting the multiple inter-reflections in the film and the substrate. Of course, such quantity must lie in the range from 0 and 1, and we can then select the unique physically meaningful solution within this range, out of the two possible mathematical results.

4. Procedure to find the Swanepoel envelopes

The previous section explained how to obtain the optical functions using our automated implementation of the Swanepoel method. Please note that the method did *not* describe how to find the envelopes from an experimental transmission spectrum or their corresponding tangent points, but rather assumed that these envelopes were known *a priori*. We now propose our novel approach to construct the envelopes and solve that initial and particularly challenging problem.

4.1. Data treatment and convexity regions

Initially, we need to select only the adequate spectral region in which the substrate exhibits negligible absorption ($k_s \approx 0$), and where the thin-layer sample has *non-zero* transmission (excluding areas of clear strong absorption), therefore confining our analysis to the spectral region valid for the Swanepoel method. We then employ a convenient Gaussian filter to reduce noise in the transmission spectrum of the sample. Finally, we interpolate the transmission curve over the full wavelength range with *cubic splines*, which ensure the second-order differentiability of the spectrum. This first step is crucial to find the tangent points with high precision, as the experimental transmittance measurements might have a relatively low spectral resolution (e.g., with measured wavelengths every 10 nm).

Following this initial data treatment, we now identify downward concave intervals within the transmission spectrum by employing the second-order numerical derivatives. The remaining spectral intervals not identified as concave are consequently categorized as upward convex intervals. Figure 5 show the convex regions in light green and the concave ones light blue. We

Optics EXPRESS

will designate the concave intervals as $[u_t^{\min}, u_t^{\max}]$, for $t \in \{1, \ldots, U\}$. Similarly, the convex intervals are denoted as $[v_t^{\min}, v_t^{\max}]$, for $t \in \{1, \ldots, V\}$. The resulting intervals must alternate, ensuring the relation $U = V \pm 1$.

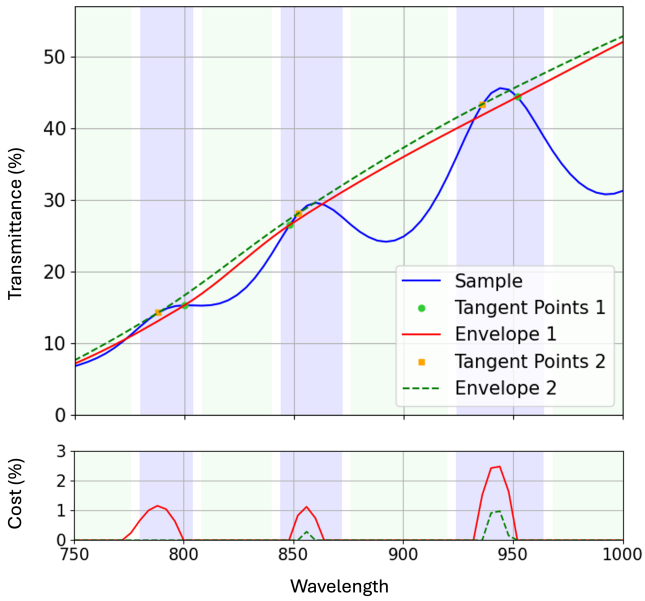


Fig. 5. Graphical illustration of the iterative optimization process used to determine the upper envelope. The algorithm identifies upper tangent points so that the interpolated curve lies entirely above the experimental transmission data, ensuring that each concave region contains a unique tangent point. During the initial iteration (red envelope), the randomly selected tangent points yield a high cost (see bottom panel). In subsequent iterations (green dashed envelope), the cost gradually decreases, allowing the solution to converge to the desired upper envelope.

Adopting the reasoning presented in [59], we will only incorporate the intervals at the end (either concave or convex) if they possess a local extremum, given that such intervals could potentially encompass a tangent point. In other words, if last interval is severely cropped, not including its minimum or maximum, it should be discarded. For instance, a short interval at the end of both graphs from Fig. 5 appears blank, as it does not contain an extrema. Additionally, the regions in the left-hand side in which $T(\lambda)$ is below a certain numerical threshold (such as 0.5%) are crop out, as no useful information about the tangent point is found in the regions of complete absorption.

In practice, noise in the transmission spectra and small absorption of the substrate typically lead to incorrect interval classification of the convexity. To compensate for this problem, we introduce a "window" variable that establishes the minimum size of the intervals (the highest frequency allowed). Intervals shorter than this window size are considered spurious and are merged with adjacent intervals to form larger, more significant regions. This process effectively filters out inconsistent high-frequency noisy oscillations in the transmission spectrum and its derivatives, ensuring that only meaningful convexity intervals are retained. The selection of this window variable must be customized depending on the unique characteristics of the experimental data and its noise.

Optics EXPRESS

4.2. Finding the tangent points with an optimization algorithm

After these steps, we formulate a global optimization problem that allows us to simultaneously determine both the tangent points and the envelopes. We incorporate into our model two essential properties of the Swanepoel envelopes, detailed below:

- **Envelopes bound the transmission curve**: The upper envelope consistently lies above the transmission curve, $T^{\text{sim}}(\lambda) \leq T_M^{\text{sim}}(\lambda)$, and the lower envelope lies below it, $T_m^{\text{sim}}(\lambda) \leq T^{\text{sim}}(\lambda)$. Consequently, the transmission curve and its envelopes touch at the tangent points but do not cross each other. This behavior follows from the definition of envelopes (see Eq. (7)) and can be readily proved under the reasonable assumption that $n \geq n_s$, which ensures the variable C in Eq. (7) is non-negative.

- **Convexity at tangent points**: Each upper tangent point is located in a concave region of the transmission curve, while each lower tangent point is found within a convex region. To justify this intuitive property, we used symbolic computation software (*Wolfram Alpha Mathematica*) to determine the second derivative of the transmission $T^{\text{sim}}(\lambda)$ at the tangent points. In spectral regions where the film exhibits medium-to-weak absorption, the optical functions $n(\lambda)$ and $k(\lambda)$ vary only slightly. It is reasonable to consider the variables (A, B, C, D, x) from Eq. (6) as approximately constant around a specific tangent point. Consequently, variations in the transmission spectrum near that point primarily stem from the term $\cos(\varphi)$ in Eq. (6), due to the rapid change of the phase $\varphi = 4\pi nd/\lambda$ with wavelength. This observation allows us to analytically estimate the derivatives of $T^{\text{sim}}(\lambda_{\text{tan}})$. We found that the second derivative is positive at the lower tangent points and negative at the upper ones.

Considering these two reasonable properties for the transmission spectra of thin uniform films, we can now define the following minimization problems:

$$\begin{cases} \text{minimize} \quad C_M(\lambda_1^M, \lambda_2^M, \ldots, \lambda_U^M) = \displaystyle\sum_{i=1}^{k} \text{ReLU}\left[T(\lambda_i) - T_M(\lambda_i; \lambda_1^M, \lambda_2^M, \ldots, \lambda_U^M)\right], \\ \text{subject to} \quad \lambda_t^M \in [u_t^{\min}, u_t^{\max}], \text{ for } t \in \{1, 2, \ldots, U\}. \end{cases} \tag{12a}$$

$$\begin{cases} \text{minimize} \quad C_m(\lambda_1^m, \lambda_2^m, \ldots, \lambda_V^m) = \displaystyle\sum_{i=1}^{k} \text{ReLU}\left[T_m(\lambda_i; \lambda_1^m, \lambda_2^m, \ldots, \lambda_V^m) - T(\lambda_i)\right], \\ \text{subject to} \quad \lambda_t^m \in [v_t^{\min}, v_t^{\max}], \text{ for } t \in \{1, 2, \ldots, V\}. \end{cases} \tag{12b}$$

Observe that non-uniform films are often modeled using a Taylor first-order approximation with a planar surface exhibiting a certain tilt. A more general expression for the transmission formula in these scenarios is derived in [33]. It should be noted that for films with a very high wedge, $\Delta d > \lambda/(4n)$, the two properties described above do no longer hold. In such cases, the upper and lower envelopes eventually cross over each other, resulting in the upper envelope lying below the spectrum with upper tangent points in convex regions (and vice versa for the lower envelope). Our current study does not apply to this more complex scenario.

The rectified linear unit (ReLU) function, frequently employed in machine learning contexts, is defined as $\text{ReLU}(x) = x$ if $x > 0$, and $\text{ReLU}(x) = 0$ if $x \leq 0$. This function ensures that the cost $C_M(\lambda_1^M, \lambda_2^M, \ldots, \lambda_n^M)$ penalizes only the instances when the upper envelope is beneath the transmission spectrum (breaking the first property), while $C_m(\lambda_1^m, \lambda_2^m, \ldots, \lambda_u^m)$ penalizes only the cases where the lower envelope is above the spectrum. Note that the constraint of the optimization problem guarantees the presence of one (and only one) upper tangent point for each concave region, and one (and only one) lower tangent point for each convex region, as established in the second property.

Optics EXPRESS

The predicted top and bottom envelopes, denoted by $T_M(\cdot)$ and $T_m(\cdot)$, are obtained using cubic Hermite interpolation [83] on the tangent points. For instance, the upper envelope corresponds to the interpolation of the points $\{\lambda_t^M, T(\lambda_t^M)\}_t$, for $t \in \{1, 2, \ldots, U\}$. Once these points are interpolated, we can evaluate the upper $T_M(\lambda)$ envelope function at any wavelength λ within the continuous spectral region, and vice-versa for the lower envelope.

The Hermite interpolation provides a piece-wise polynomial approximation of the envelopes, while maintaining monotonicity within each piece. By utilizing cubic Hermite interpolation, we not only ensure that the interpolated envelopes pass through the given tangent points but also that they conform to the specific slopes at those points. This method incorporates both the function values and their first derivatives, resulting in a piecewise cubic polynomial that is continuous in both value and slope. The inclusion of derivative information allows the interpolation to capture the local behavior of the data more accurately, preserving essential features such as peaks and inflection points. Moreover, cubic Hermite interpolation minimizes oscillations between data points, a common issue with higher-degree polynomial interpolations that do not consider slope information. This reduction in unwanted oscillatory behavior leads to a more stable and reliable approximation of the envelopes.

To solve the optimization problems presented in Eqs. (12a–12b), we utilize the Simulated (Dual) Annealing algorithm [80]. It should be noted that conventional local optimizers (such as Gradient-Descent, Levenberg-Marquardt, or Nelder-Mead), fail to converge to the correct solution due to the presence of several local minima. Very significantly, our algorithm converges in 30-60 seconds on a standard computer, given the simplicity of the cost functions. Figures 6(a)-b show a the results of our envelope-detection algorithm for a simulated sample and a zoom-in of the strong-absorption region. Figures 6(c)-d show the results of our approach for the real samples #1 and #2, respectively.

4.3. Boundary points

Interpolation near the edges of the spectral region of interest (ROI) can be challenging, particularly at the first and last tangent points. To improve accuracy, we propose extending the envelope calculation to include boundary points at both ends of the ROI rather than stopping at the first and last tangent points. This ensures that the first and last tangent points become interior nodes rather than endpoints, improving the stability of the interpolation. The selection of boundary points is informed by the film's behavior at both extremes of the spectrum.

First boundary point(s): At shorter wavelengths, where absorption is strong, the amplitude of the oscillations decrease, and the upper and lower envelopes converge toward the measured transmittance $T(\lambda_{\text{init}}) \approx 0$, indicating that the film is essentially opaque (see Fig. 6(a) below 600 nm). Thus, an additional boundary node $(\lambda_{\text{init}}, T(\lambda_{\text{init}}))$ is placed at the initial wavelength for both the upper and lower envelopes. In cases where the region of near-complete absorption is not fully cropped, one can place this boundary node at the earliest wavelength where $T(\lambda_{\text{init}}) \approx 0$ still holds true. One can see these first two added boundary points in Fig. 6(a).

Last boundary point: At longer wavelengths, where absorption weakens and the envelopes flatten, we approximate the last boundary point $(\lambda_{\text{last}}, y_{\text{last}})$ using a simple parabolic model based on the *two final tangent points*, denoted (λ_1, y_1) and (λ_2, y_2). In this ending region, the tangent points indeed lie very close to the local extrema, making this approximation convenient in practice. Specifically, we assume the mathematical model:

$$y_{\text{last}} = T_0 + \frac{T_1}{\lambda - \lambda_0}, \tag{13}$$

Where the amplitude $T_1 \in [0, 1]$ and wavelength λ_0 are determined analytically from the two last maxima (λ_1, y_1) and (λ_2, y_2) for the upper envelope, or minima for the lower envelope. The parameter T_0 is fix to the mean substrate absorption T_s in the case of the upper envelope: in

Optics EXPRESS

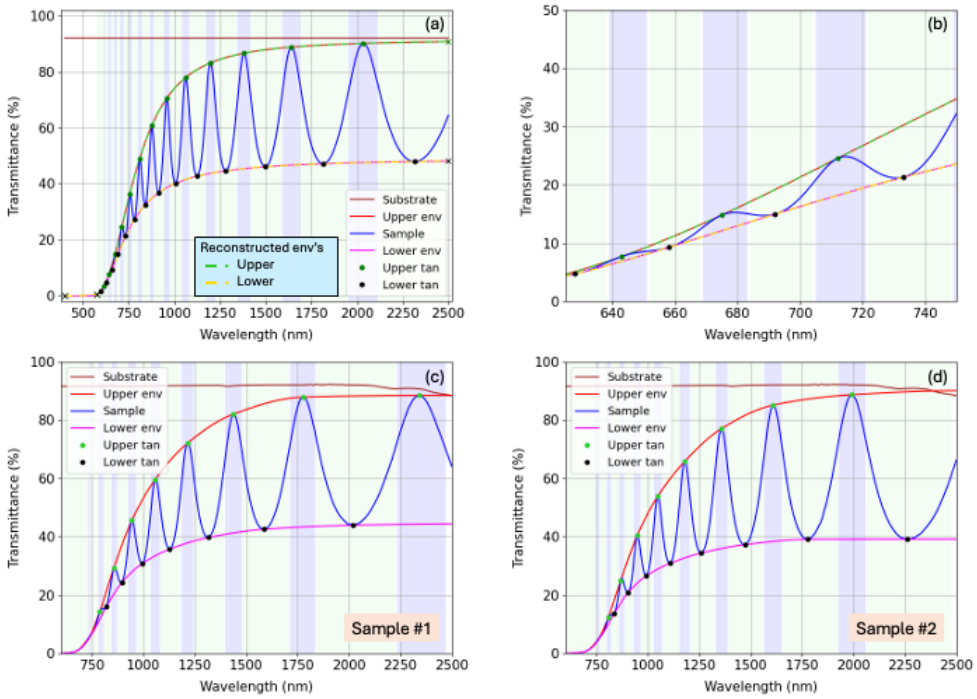


Fig. 6. Envelopes and tangent points determined using our novel optimization procedure. In particular, (a) shows the reconstructions for simulated sample and (b) a magnified view of its strong absorption region, while (c) and (d) show transmittance curves for the real samples #1 and #2, respectively. These results satisfy the two constraints imposed in our optimization problem: first, the upper (lower) envelope consistently lies above (below) the transmittance curve, touching it only at upper (lower) tangent points; second, these tangent points are localized within the light-blue concave (upper) or light-green convex (lower) regions.

the weak absorption region, the upper envelope naturally converges to the almost flat curve of the transmittance. In the case of the lower envelope, we calculate the distance between the last maximum and minimum values, which approximates $T_{\mathrm{M}}^{-1} - T_{\mathrm{m}}^{-1}$ at the end of the spectrum. We then know that, in the region of weak absorption, the lower envelope must eventually convergent for longer wavelengths to the value $T_0 = T_{\mathrm{s}} - (T_{\mathrm{M}}^{-1} - T_{\mathrm{m}}^{-1})$.

By integrating this physically informed boundary treatment, we ensure a smoother and more reliable envelope estimation across the entire ROI. Note that alternative boundary conditions may be employed for other type of spectra, such as those not reaching near-zero transmittance at the short-wavelength limit, not approaching a medium-to-weak region at the long-wavelength end, or reaching the completely non-absorption region at the long-wavelength end. Our implementation allows users to select different boundary models, such as a flat envelope at the long-wavelength side when complete transparency is reached, exponential and linear fits from the two first or last tangent points, and even manual selection, for more pathological cases.

5. Other envelope construction techniques

We now present an overview of three envelope construction approaches, including (i) the widely employed McClain iterative algorithm [59], (ii) the practical parabolic or exponential fitting methods, and the recently devised (iii) deep learning technique [70], all of which will serve as benchmarks for evaluating our approach in the subsequent section. The implementation of other

Optics EXPRESS

methodologies proposed in the literature [63–66], for which no openly available code exists, is beyond the scope of this study.

5.1. McClain algorithm

The most widely employed and established algorithm for envelope construction was developed by McClain et al. in 1991 [59]. This technique consists of two distinct phases: first estimating the tangent points and then refining them.

In the *first* phase, one identifies the local minima and maxima of the transmission curve, tentatively assigning them as the lower and upper tangent points. Since not all tangent points coincide with peaks and valleys, an alternative approach involves selecting the midpoints of the concave and convex regions. These estimated tangent points are then used to construct the first approximated lower and upper envelopes via B-spline interpolation. The initial estimation of the tangent points during the first phase is the most critical part to find accurate envelopes.

Observe that the algorithm requires the first and last tangent points, located at the boundaries of the interval, to coincide with local extrema (i.e., maxima for the upper envelope and minima for the lower envelope). While this approach helps avoid including invalid or spurious points, as noted in the seminal Ref. [59], it also leads to drawbacks. For one, it may produce larger errors, as evidenced by the substantial shift from the first extremum to the corresponding tangent point (see Fig. 1(d)). Moreover, it excludes many potentially useful tangent points in the shorter-wavelength region where small oscillations often occur without forming clear local maxima or minima. In broadband transmission measurements, the spectrum typically transitions from strong absorption near the optical bandgap to moderate or weak absorption further away. Early in the spectrum, small oscillations frequently arise without distinct local extrema. By requiring that the first tangent point be a local extremum, the algorithm effectively discards these non-extremal oscillations, undermining the intended benefit of using the midpoints of concave/convex intervals instead of the peaks/valleys as initial tangent point candidates.

In the *second* phase, the algorithm iteratively refines the tangent points to improve the accuracy of the envelopes. Focusing on the upper envelope, the algorithm identifies "incorrect" regions in which the estimated upper envelope $T_M(\lambda)$ falls below the actual transmission spectrum $T(\lambda)$. The upper tangent points are then relocated to the midpoints of these incorrect regions, as done in the bisection method. A new upper envelope is recalculated based on the updated tangent points. This iterative process is repeated until convergence (or up to a maximum of 20 times), progressively reducing the size of the incorrect regions at each step. Note that the same refinement procedure is applied to the lower tangent points and envelope. In this case, the incorrect regions are those where the estimated lower envelope $T_m(\lambda)$ lies above the transmission spectrum $T(\lambda)$.

5.2. Parabolic or exponential fitting

Another prevalent technique involves the direct fitting of local maxima (or minima) using either parabolic or exponential curves to construct the upper (or lower) envelopes. The envelopes then follow one of these mathematical expressions:

$$f^{\text{para}}(\lambda; T_0, T_1, T_2, \Lambda_1, \Lambda_2) = T_0 + \frac{10^2 \cdot T_1}{\lambda - \Lambda_1} + \frac{10^5 \cdot T_2}{(\lambda - \Lambda_2)^2} \tag{14a}$$

$$f^{\text{exp}}(\lambda; T_0, T_1, T_2, \Lambda_1, \Lambda_2) = T_0 + T_1 \cdot e^{-\lambda/\Lambda_1} + T_2 \cdot e^{-\lambda/\Lambda_2} \tag{14b}$$

The optimal parameters $(T_0, T_1, T_2, \Lambda_1, \Lambda_2)$ can be obtained by solving a nonlinear least-square fitting problem. Although generally less precise than McClain algorithm, it is crucial to point out that this fitting approach is notably beneficial for transmission spectra that exhibit a restricted number of oscillations and tangent points, a condition often encountered with ultra-thin films.

Optics EXPRESS

The piece-wise interpolations used in both the McClain algorithm and our newly proposed methods typically require at least four tangent points for a reliable estimation of each envelope.

The fitting method has also proved valid [67] for crystalline film materials, where the materials present a distinct absorption band and are almost transparent beyond the absorption region. These materials have an almost nonexistent Urbach tail, given their low level of molecular disorder. In this cases, the subsequent very flat envelope curves can be conveniently modeled by Eqs. (14a–14b), independently of the amount of present oscillations in the transmission spectrum.

Our method introduces the artificial boundary points at the ends of the spectral range using a similar approach, but applying first-order parabolic or exponential functions rather than a second-order ones. This adjustment ensures that the fitting procedure is well-defined and depends only on the final two nodes, enabling a direct analytical solution.

5.3. Deep learning approach

While both McClain and the curve-fitting algorithms offer reasonable outcomes in practice and converge to an envelope of an oscillating function, they do not necessarily converge to the exact expression of the Swanepoel envelopes, as defined in Eq. (8). To overcome this issue, our group developed a deep learning (DL) approach [70] that calculates the envelopes in alignment with the Swanepoel theoretical expressions. In particular, we created a dataset of 100,000 input-output pairs $\{T(\lambda), T_M(\Lambda)\}$ for training using the exact Eqs. (6 –8a). A supervised convolutional neural networks (CNNs) model was trained with this dataset to predict the upper and lower envelopes from a transmission spectrum in real-time. While this DL model does not have limitations on the number of tangent points, it is susceptible to noise and artifacts from real-world transmission measurements. This is caused because the distribution of the simulated data differs significantly, which is a known issue for DL approaches used in inverse problems like image restoration or super-resolution [84–87].

The noise in real measures strongly depends on the instrumentation and the conditions of the particular experiment. For instance, one potential sources of deviance between the simulated and real spectra is the photodetector noise, which can be responsible up to the 0.2% transmittance error. Second, the effect of the realistic limited coherent length of the beam in the thin film, which affects the peaks and valleys. Third, the increase of coherent length with the wavelength, which may eventually lead to the high frequency noise due to the undesired thick-substrate interferences. Fourth, the change in the emitting source for UV versus VIS-NIR, which may produces a significant jump in the transmittance. Fifth, the substrate absorption of at particular wavelengths, and the absorption of air components if the experiment is not carefully performed in a vacuum. Observe that modeling these noise sources in general is challenging and not yet fully addressed in the current literature. Incorporating a comprehensive theoretical noise model could enhance the current DL approach by providing deeper insights and improving its overall performance with real data.

6. Validation and comparison

We began by validating our envelope construction procedure using 50 computer-generated transmission spectra, each accompanied by a known theoretical envelope. In particular, we generated 50 random set of parameters $(d, E_0, E_\mathrm{d}, \alpha_0, E_\mathrm{u})$ within the bounds specified in Table 1. These data were then employed in Eq. (6) to produce the transmittance, and Eqs. (8a)–(8b) for their corresponding envelopes. The substrate transmittance is assumed constant, with the typical value $T_\mathrm{s} = 92\%$.

Accurate envelope determination relies on the inclusion of boundary points. For the first boundary point, corresponding to a regime of nearly complete absorption ($T \approx 0$), the estimation is straightforward in our simulated samples, as the chosen spectral range encompasses the strongly absorbing region near the band gap. In contrast, determining the last boundary point is a more

Optics EXPRESS

challenging task. Comparison of our default parabolic-fitting model with the known ground-truth last boundary point resulted in a transmittance error of 0.143 ± 0.214% for the upper boundary point and 0.142 ± 0.125% for the lower boundary point.

Applying our envelope detection procedure to the simulated spectra yielded an RMSE of 0.098 ± 0.084% for the upper envelope and 0.058 ± 0.045% for the lower envelope. The slightly higher RMSE for the upper envelope is attributed to its intrinsically larger values. Notably, *all* tangent points were correctly identified, with an average absolute error of 1.06 ± 0.95 nm for the upper tangent points and 2.99 ± 2.62 nm for the lower tangent points. Table 3 compares our method performance to that of the standard McClain algorithm. Because McClain method identifies only tangent points associated with local extrema, the spectral range in which it computes the envelopes is considerably shorter than the full region of interest. To ensure a fair comparison, we restrict both methods to the same shorter spectral region. Our method achieves less than half the RMSE for the envelopes and an absolute error on tangent point location that is about an order of magnitude smaller.

Table 3. Comparing our proposed method with respect to the standard McClain algorithm within the same spectral region (between the first and last local extrema).

Method	Upper env.	Lower env.	Upper tan	Lower tan
McClain	0.202 ± 0.129	0.090 ± 0.040	2.59 ± 1.75	2.48 ± 1.45
Ours	0.080 ± 0.078	0.043 ± 0.034	0.27 ± 0.33	0.55 ± 0.72

For a further comparison with curve-fitting approaches, we restrict analysis to spectra with fewer than five tangent points associated with extrema and generate 50 computer-simulated spectra by varying the sample thickness from 200 to 500 nm only, considering ultra-thin film samples. The reported RMSE for the envelopes is computed between the first and last identified tangent points. Under these conditions, the exponential fit yields an error of 2.11% for the upper envelope and 0.31% for the lower envelope, whereas the parabolic fit produces errors of 1.19% (upper) and 0.42% (lower). Because the tangent points in these fits are directly (and somewhat imprecisely) tied to local extrema, their errors increase considerably: 6.10 nm for the exponential fit and 7.66 nm for the parabolic fit. As noted previously, the DL algorithm achieves very low errors (0.14% for the upper and 0.05% for the lower envelopes) over the entire spectral range, but it remains incompatible with realistic noisy data and does not directly provide the locations of the tangent points.

It is important to recognize that the exact optical properties and ground-truth envelopes are obviously unavailable for the case of real spectra, unlike the case with simulated data. To address this limitation, we leverage the results of inverse synthesis as a benchmark for assessing the optical characterization analysis performed by `swanpy`. This comparison should thus be viewed as a *consistency check* rather than a strict accuracy evaluation.

1. First, Fig. 7 shows good agreement between the optical functions n and k extracted via inverse synthesis (continuous curves) and those evaluated at specific tangent points by our improved Swanepoel method.

2. Second, the Swanepoel method demonstrates reliable accuracy for determining film thickness. As shown in Table 2, sample #1 exhibits a relative thickness error of 0.65%, while sample #2 has an error of 0.90%. Notably, the thicknesses from inverse synthesis (d = 1117 nm for sample #1 and d = 1160 nm for sample #2) both lie within the corresponding Swanepoel confidence intervals (d = 1110 ± 7 nm for sample #1 and d = 1163 ± 11 nm for sample #2).

3. Third, an indirect but informative way to validate envelope detection in real measurements is to analyze the interference orders from Table 2. We find that the computed orders m lie

Optics EXPRESS

very close to half-integer values (columns 6 and 7), indicating an accurate determination of tangent points and envelopes. When misidentified tangent points do occur, their associated interference orders tend to align with other half-integer values rather than the expected one.

This consistency across multiple metrics supports the robustness of our approach for real experimental data.

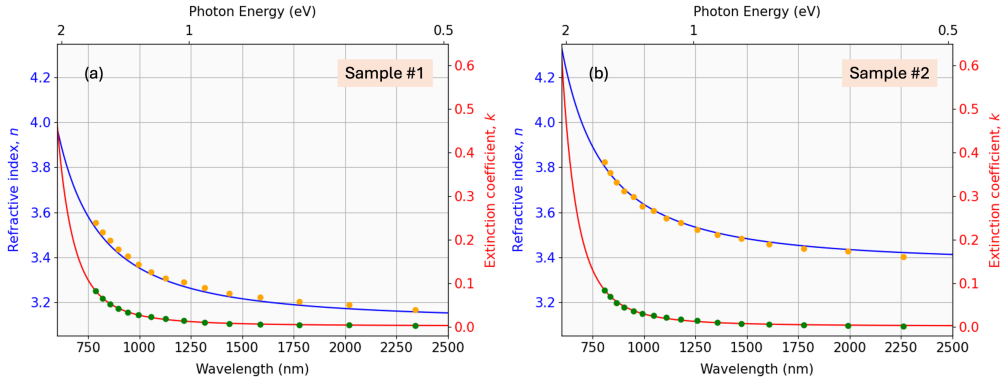


Fig. 7. Refractive index and extinction coefficient for *a*-Si samples #1 and #2, found with the inverse synthesis approach (solid lines) and with our proposed improved Swanepoel method (circles).

7. Conclusions

In this work, we present a novel algorithm for Swanepoel envelopes construction, an essential aspect in the optical characterization of thin films. Our approach integrates the physical properties of the Swanepoel envelopes into a global optimization problem. After evaluation with fifty computer-generated spectra, our algorithm demonstrated an RMSE below 0.01% for the upper envelope and 0.06% for the lower envelope, significantly surpassing the performance of existing state-of-the-art methods. We also successfully applied our approach to characterize two real samples of amorphous silicon.

Additionally, we integrated our envelope construction algorithm with our automated implementation of the Swanepoel method in an open-source Python package, `swanpy`. Given its noise robustness, high accuracy, and speed, our program emerges as a valuable tool for the optical characterization of thin solid films. It should be noted that the envelope construction presented in this work can be coupled with more advanced envelope methods. Therefore, future research could explore the applicability of our approach in more complex and realistic films, such as those with non-uniform thickness, multi-layer samples, or absorbent substrates.

Disclosures. The authors declare no conflicts of interest.

M.B. developed the method and the wrote the draft of the manuscript. S.L-T. and A.P.M. developed the software. S.F. provided the experimental data. J.B., D.M., and C.W. made revisions of the manuscript and validated the results. F.W., E.M., and A.K.K. conceptualized the idea and supervised the project. All authors reviewed and approved the manuscript.

Data Availability. All data underlying the results presented in this paper are available in the link provided within the text.

References

1. E. Fortunato, P. Barquinha, and R. Martins, "Oxide semiconductor thin-film transistors: a review of recent advances," Adv. Mater. **24**(22), 2945–2986 (2012).
2. N. A. Al-Ahmadi, "Metal oxide semiconductor-based schottky diodes: a review of recent advances," Mater. Res. Express **7**(3), 032001 (2020).

Optics EXPRESS

3. L. Sang, M. Liao, and M. Sumiya, "A comprehensive review of semiconductor ultraviolet photodetectors: from thin film to one-dimensional nanostructures," Sensors **13**(8), 10482–10518 (2013).
4. V. H. López-Lugo, M. García-Hipólito, A. Rodríguez-Gómez, *et al.*, "Fabrication of li-doped nio thin films by ultrasonic spray pyrolysis and its application in light-emitting diodes," Nanomaterials **13**(1), 197 (2023).
5. M.-J. Spijkman, K. Myny, E. C. Smits, *et al.*, "Dual-gate thin-film transistors, integrated circuits and sensors," Adv. Mater. **23**(29), 3231–3242 (2011).
6. J. Henry and J. Livingstone, "Thin-film amorphous silicon position-sensitive detectors," Adv. Mater. **13**(12-13), 1022–1026 (2001).
7. Y. S. Rim, "Review of metal oxide semiconductors-based thin-film transistors for point-of-care sensor applications," J. Inf. Disp. **21**(4), 203–210 (2020).
8. A. Shah, R. Platz, and H. Keppner, "Thin-film silicon solar cells: a review and selected trends," Sol. energy materials solar cells **38**(1-4), 501–520 (1995).
9. M. Ballester, A. Márquez, C. García-Vázquez, *et al.*, "Energy-band-structure calculation by below-band-gap spectrophotometry in thin layers of non-crystalline semiconductors: A case study of unhydrogenated a-si," J. Non-Cryst. Solids **594**, 121803 (2022).
10. A. J. Lopez-Garcia, G. Alvarez-Suarez, E. Ros, *et al.*, "Enhanced selective contact behavior in a-si: H/oxide transparent photovoltaic devices via dipole layer integration," Sol. RRL **8**(14), 2400276 (2024).
11. E. Maiorano, S. Gianvittorio, M. Lanzi, *et al.*, "Print-light-synthesis of gold thin film electrodes for electrochemical sensing," Adv. Mater. Technol. **8**(12), 2202039 (2023).
12. M. G. Toudeshkchoui, N. Rabiee, M. Rabiee, *et al.*, "Microfluidic devices with gold thin film channels for chemical and biomedical applications: a review," Biomed. Microdevices **21**(4), 93 (2019).
13. M. M. Singh, G. Vijaya, M. Krupashankara, *et al.*, "Deposition and characterization of aluminium thin film coatings using dc magnetron sputtering process," Mater. Today: Proc. **5**(1), 2696–2704 (2018).
14. W. He and C. Ye, "Flexible transparent conductive films on the basis of ag nanowires: design and applications: a review," J. Mater. Sci. & Technol. **31**(6), 581–588 (2015).
15. J. P. Silva, K. C. Sekhar, H. Pan, *et al.*, "Advances in dielectric thin films for energy storage applications, revealing the promise of group iv binary oxides," ACS Energy Lett. **6**(6), 2208–2217 (2021).
16. R. Politanskyi, M. Vistak, G. Barylo, *et al.*, "Simulation of anti-reflecting dielectric films by the interference matrix method," Opt. Mater. **102**, 109782 (2020).
17. M. Kumar, N. Kumari, P. K. Rao, *et al.*, "Multi-layer dielectric thin-film optical filters for beam folding applications," in *International Conference on Optics and Photonics 2015*, vol. 9654 (SPIE, 2015), pp. 90–94.
18. J. Benedikt, V. Raballand, A. Yanguas-Gil, *et al.*, "Thin film deposition by means of atmospheric pressure microplasma jet," Plasma Phys. Controlled Fusion **49**(12B), B419–B427 (2007).
19. F. Massines, C. Sarra-Bournet, F. Fanelli, *et al.*, "Atmospheric pressure low temperature direct plasma technology: status and challenges for thin film deposition," Plasma Process. Polym. **9**(11-12), 1041–1073 (2012).
20. A. Tumuluri, K. L. Naidu, and K. J. Raju, "Band gap determination using tauc's plot for linbo3 thin films," Int. J. ChemTech Res **6**, 3353–3356 (2014).
21. J. Guerra, A. Tejada, J. Töfflinger, *et al.*, "Band-fluctuations model for the fundamental absorption of crystalline and amorphous semiconductors: a dimensionless joint density of states analysis," J. Phys. D: Appl. Phys. **52**(10), 105303 (2019).
22. M. Bhowmick, H. Xi, and B. Ullrich, "Optical bandgap definition via a modified form of urbach's rule," Materials **14**(7), 1639 (2021).
23. C. Kaiser, O. J. Sandberg, N. Zarrabi, *et al.*, "A universal urbach rule for disordered organic semiconductors," Nat. Commun. **12**(1), 3988 (2021).
24. N. Ueno and S. Kera, "Electron spectroscopy of functional organic thin films: Deep insights into valence electronic structure in relation to charge transport property," Prog. Surf. Sci. **83**(10-12), 490–557 (2008).
25. J. Park, Y. J. Cho, W. Chegal, *et al.*, "A review of thin-film thickness measurements using optical methods," Int. J. Precis. Eng. Manuf. **25**(8), 1725–1737 (2024).
26. H. Fujiwara, *Spectroscopic Ellipsometry: Principles and Applications* (John Wiley & Sons, 2007).
27. E. Márquez, E. Blanco, J. M. Mánuel, *et al.*, "Mid-infrared (mir) complex refractive index spectra of polycrystalline copper-nitride films by ir-vase ellipsometry and their fib-sem porosity," Coatings **14**(1), 5 (2023).
28. R. Swanepoel, "Determination of the thickness and optical constants of amorphous silicon," J. Phys. E: Sci. Instrum. **16**(12), 1214–1222 (1983).
29. J. F. Hall and W. Ferguson, "Optical properties of cadmium sulfide and zinc sulfide from 0.6 micron to 14 microns," J. Opt. Soc. Am. **45**(9), 714–718 (1955).
30. S. Lyashenko and V. Miloslavsky, "A simple method for semiconductor and dielectric layers thickness and optical constants determining," Optika i Spektroskopiya **16**, 151 (1964).
31. J. Manifacier, J. Gasiot, and J. Fillard, "A simple method for the determination of the optical constants n, k and the thickness of a weakly absorbing thin film," J. Phys. E: Sci. Instrum. **9**(11), 1002–1004 (1976).
32. H. Liu, D. Hou, Z. Wang, *et al.*, "Comparison of envelope method and full spectra fitting method for determination of optical constants of thin films," in *Seventh International Conference on Thin Film Physics and Applications*, vol. 7995 (SPIE, 2011), pp. 381–384.

Optics EXPRESS

33. M. Ballester, E. Marquez, J. Bass, *et al.*, "Review and novel formulae for transmittance and reflectance of wedged thin films on absorbing substrates," arXiv (2024).
34. R. Swanepoel, "Determination of surface roughness and optical constants of inhomogeneous amorphous silicon films," J. Phys. E: Sci. Instrum. **17**(10), 896–903 (1984).
35. R. Swanepoel, "Determining refractive index and thickness of thin films from wavelength measurements only," J. Opt. Soc. Am. A **2**(8), 1339–1343 (1985).
36. D. Kushev, N. Zheleva, Y. Demakopoulou, *et al.*, "A new method for the determination of the thickness, the optical constants and the relaxation time of weakly absorbing semiconducting thin films," Infrared Phys. **26**(6), 385–393 (1986).
37. R. Swanepoel, "Transmission and reflection of an absorbing thin film on an absorbing substrate," South African Journal of Physics **12**, 148–156 (1989).
38. M. Nowak, "Determination of optical constants and average thickness of inhomogeneous-rough thin films using spectral dependence of optical transmittance," Thin Solid Films **254**(1-2), 200–210 (1995).
39. X. Wu, F. Lai, L. Lin, *et al.*, "Optical inhomogeneity of zns films deposited by thermal evaporation," Appl. Surf. Sci. **254**(20), 6455–6460 (2008).
40. Y. Jin, B. Song, Z. Jia, *et al.*, "Improvement of swanepoel method for deriving the thickness and the optical properties of chalcogenide thin films," Opt. Express **25**(1), 440–451 (2017).
41. Y. Jin, B. Song, C. Lin, *et al.*, "Extension of the swanepoel method for obtaining the refractive index of chalcogenide thin films accurately at an arbitrary wavenumber," Opt. Express **25**(25), 31273–31280 (2017).
42. J. Dobrowolski, F. Ho, and A. Waldorf, "Determination of optical constants of thin film coating materials based on inverse synthesis," Appl. Opt. **22**(20), 3191–3200 (1983).
43. N. Kamble, R. Tokas, A. Biswas, *et al.*, "Determination of the optical constants of hfo2–sio2 composite thin films through reverse fitting of transmission spectra," Vacuum **86**(4), 422–428 (2011).
44. Z. Hu, Z. Huang, Z. Lai, *et al.*, "Optical properties of amorphous pbzrxti1- xo3 (x= 0.52) thin films prepared by rf magnetron sputtering," Thin Solid Films **437**(1-2), 223–229 (2003).
45. Z. E. Hebal, N. Sengouga, A. Meftah, *et al.*, "Development of a software "hebaloptics" to extract optical properties and thickness of thin films from a single transmittance measurement," Opt. Quantum Electron. **56**(10), 1660 (2024).
46. M. Ballester, A. P. Márquez, S. Banerjee, *et al.*, "Comparison of optical characterization methods for transmission spectroscopy," in *Computational Optical Sensing and Imaging*, (Optica Publishing Group, 2022), pp. JW5D–4.
47. D. Poelman and P. Smet, "Methods for the determination of the optical constants of thin films from single transmission measurements: A critical review," J. Phys. D: Appl. Phys. **36**(15), 1850–1857 (2003).
48. M. Ballester, M. García, A. P. Márquez, *et al.*, "Application of the holomorphic tauc-lorentz-urbach function to extract the optical constants of amorphous semiconductor thin films," Coatings **12**(10), 1549 (2022).
49. A. Ferlauto, G. Ferreira, J. M. Pearce, *et al.*, "Analytical model for the optical functions of amorphous semiconductors from the near-infrared to ultraviolet: Applications in thin film photovoltaics," J. Appl. Phys. **92**(5), 2424–2436 (2002).
50. L. V. Rodríguez-de Marcos and J. I. Larruquert, "Analytic optical-constant model derived from tauc-lorentz and urbach tail," Opt. Express **24**(25), 28561–28572 (2016).
51. J. I. Larruquert and L. V. Rodríguez-de Marcos, "Procedure to convert optical-constant models into analytic," Thin Solid Films **664**, 52–59 (2018).
52. J. I. Larruquert and L. V. Rodríguez-de Marcos, "Corrigendum to procedure to convert optical-constant models into analytic thin solid films (2018) 52-59," Thin Solid Films **733**, 138816 (2021).
53. D. Franta, D. Nečas, and I. Ohlídal, "Universal dispersion model for characterization of optical thin films over a wide spectral range: application to hafnia," Appl. Opt. **54**(31), 9108–9119 (2015).
54. D. Franta, D. Nečas, A. Giglia, *et al.*, "Universal dispersion model for characterization of optical thin films over wide spectral range: Application to magnesium fluoride," Appl. Surf. Sci. **421**, 424–429 (2017).
55. D. Franta and M.-G. Mureşan, "Wide spectral range optical characterization of yttrium aluminum garnet (yag) single crystal by the universal dispersion model," Opt. Mater. Express **11**(12), 3930–3945 (2021).
56. D. Franta, J. Vohánka, J. Dvořák, *et al.*, "Optical characterization of gadolinium fluoride films using universal dispersion model," Coatings **13**(2), 218 (2023).
57. M. Ballester, C. Würsch, E. Marquez, *et al.*, "Optical characterization of thin films from transmission data using deep learning," in *Quantum Sensing and Metrology*, (Optica Publishing Group, 2024), pp. FD1–1.
58. J. M. Bass, M. Ballester, S. M. Fernández, *et al.*, "An angular spectrum approach to inverse synthesis for the characterization of optical and geometrical properties of semiconductor thin films," arXiv (2024).
59. M. McClain, A. Feldman, D. Kahaner, *et al.*, "An algorithm and computer program for the calculation of envelope curves," Comput. Phys. **5**(1), 45–48 (1991).
60. M. H. Saleh, N. M. Ershaidat, M. J. A. Ahmad, *et al.*, "Evaluation of spectral dispersion of optical constants of a-se films from their normal-incidence transmittance spectra using swanepoel algebraic envelope approach," Opt. Rev. **24**(3), 260–277 (2017).
61. B. S. Richards, "Optical characterization of sputtered silicon thin films for photovoltaic application," Ph.D. thesis, MSc. Thesis (1998).
62. T. Güngör and B. Saka, "Calculation of the optical constants of a thin layer upon a transparent substrate from the reflection spectrum using a genetic algorithm," Thin Solid Films **467**(1-2), 319–325 (2004).

Optics EXPRESS

63. D. Minkov and R. Swanepoel, "Computerization of the optical characterization of a thin dielectric film," Opt. Eng. **32**(12), 3333–3337 (1993).
64. D. Minkov and R. Swanepoel, "Computer drawing of the envelopes of spectra with interference," in *Thin Films for Optical Systems*, vol. 1782 (SPIE, 1993), pp. 212–220.
65. G. Gavrilov, D. Minkov, E. Marquez, *et al.*, "Advanced computer drawing envelopes of transmittance spectra of thin film specimens," spectrum **5**, 6 (2016).
66. D. A. Minkov, G. M. Gavrilov, E. Marquez, *et al.*, "Development of algorithm for computer drawing envelopes of interference reflectance spectra for thin film specimens," Optik **132**, 320–328 (2017).
67. M. Salah, A. Abdelnaeim, S. Makhlolf, *et al.*, "Optical parameters of varies thickness of bismuth (iii) iodide thin films for photovoltaic and nonlinear applications," Int. J. Thin. Film. Sci. Tec. **11**(3), 275–282 (2022).
68. V. Matějec, J. Pedliková, I. Barton, *et al.*, "Optical properties of as2s3 layers deposited from solutions," J. Non-Cryst. Solids **431**, 47–51 (2016).
69. D. Dorranian, L. Dejam, and G. Mosayebian, "Optical characterization of cu 3 n thin film with swanepoel method," J. Theor. Appl. Phys. **6**(1), 1–9 (2012).
70. M. Ballester, E. Marquez, A. P. Marquez, *et al.*, "Deep learning method to find swanepoel envelopes in transmission spectroscopy," in *Computational Optical Sensing and Imaging*, (Optica Publishing Group, 2023), pp. CTh2A–5.
71. M. Ballester "swanpy," Google, 2024https://drive.google.com/drive/folders/1OdwJavus-JI2IMM81442716FFytGiCZ3.
72. M. Born and E. Wolf, *Principles of optics: electromagnetic theory of propagation, interference and diffraction of light* (Elsevier, 2013).
73. D. J. Borah and A. Mostako, "Investigation on dispersion parameters of molybdenum oxide thin films via wemple–didomenico (wdd) single oscillator model," Appl. Phys. A **126**(10), 818 (2020).
74. B. Ullrich, A. K. Singh, M. Bhowmick, *et al.*, "Photoluminescence lineshape of zno," AIP Adv. **4**(12), 123001 (2014).
75. E. Marquez, J. Gonzalez-Leal, R. Prieto-Alcon, *et al.*, "On the photo-and thermally-induced darkening phenomena in as40 s40 se20 amorphous chalcogenide thin films," J. Phys. D: Appl. Phys. **32**(24), 3128–3134 (1999).
76. K. Tanaka, "Optical properties and photoinduced changes in amorphous ass films," Thin Solid Films **66**(3), 271–279 (1980).
77. M. Foldyna, K. Postava, J. Bouchala, *et al.*, "Model dielectric functional of amorphous materials including urbach tail," in *Microwave and Optical Technology 2003*, vol. 5445 (SPIE, 2004), pp. 301–305.
78. N. Malkova, L. Poslavsky, M. Di, *et al.*, "New dispersion model for band gap tracking," Thin Solid Films **595**, 32–35 (2015).
79. E. Garoudja, R. Amrani, W. Filali, *et al.*, "Artificial bee colony algorithm: a novel strategy for optical constants and thin film thickness extraction using only optical transmittance spectra for photovoltaic applications," Optik **241**, 167030 (2021).
80. P. Virtanen, R. Gommers, T. E. Oliphant, *et al.*, "SciPy 1.0: Fundamental algorithms for scientific computing in Python," Nat. Methods **17**(3), 261–272 (2020).
81. J. Gonzalez-Leal, M. Stuchlik, M. Vlcek, *et al.*, "Influence of the deposition technique on the structural and optical properties of amorphous ass films," Appl. Surf. Sci. **246**(4), 348–355 (2005).
82. E. Hecht, *Optics* (Pearson Education India, 2012).
83. R. P. Canale and S. C. Chapra, *Numerical methods for engineers* (Mcgraw-hill Education-Europe, 2014).
84. Y. Yuan, S. Liu, J. Zhang, *et al.*, "Unsupervised image super-resolution using cycle-in-cycle generative adversarial networks," *2018 IEEE/CVF Conference on Computer Vision and Pattern Recognition Workshops (CVPRW)* pp. 814–81409 (2018).
85. K. Zhang, W. Zuo, and L. Zhang, "Deep plug-and-play super-resolution for arbitrary blur kernels," in *IEEE Conference on Computer Vision and Pattern Recognition*, (2019).
86. J. Cai, H. Zeng, H. Yong, *et al.*, "Toward real-world single image super-resolution: A new benchmark and a new model," in *Proceedings of the IEEE/CVF International Conference on Computer Vision (ICCV)*, (2019).
87. S. López-Tapia, J. Mateos, R. Molina, *et al.*, "Learning moore-penrose based residuals for robust non-blind image deconvolution," Digit. Signal Process. **142**, 104193 (2023).

150.214.75.244 2025-10-28 15:27:1